PROCEEDINGS, 42nd Workshop on Geothermal Reservoir Engineering
Stanford University, Stanford, California, February 13-15, 2017
SGP-TR-212

Comparison of Experimental and Modeling Results of Fracture Sustainability in EGS Systems

Timothy J. Kneafsey, Seiji Nakagawa, Eric L. Sonnenthal, Marco Voltolini, Patrick F. Dobson, J. Torquil Smith, Sharon E. Borglin

Lawrence Berkeley National Laboratory, Earth and Environmental Sciences, 1 Cyclotron Road, Berkeley, CA, 94720 USA

tjkneafsey@lbl.gov

Keywords: engineered geothermal systems, fracture, dissolution, precipitation, experimental, modeling

ABSTRACT

Asperities resulting from shear offsets in fractures prop the fractures open and are key to providing permeability in enhanced geothermal systems (EGS). These asperities and the resulting permeability are controlled by rock dissolution, precipitation, and mechanical deformation. These in turn are functions of the temperature, pressure, fluid chemistry, mineralogy, and stress state of the system. Fracture permeability changes under the conditions that could be expected in EGS reservoirs have been quantified in our laboratory experiments. Through experiments our objective has been to gain a better understanding of how different rock types, mineral compositions, and fracture surface topography affect the life span of fractures, enabling selection of reservoir rock to optimize long-term fracturing effectiveness. Through modeling, we aim to extend these results.

Our experimental tests were performed in a custom laboratory apparatus which applies normal stress on a disk-shaped rock sample containing a fracture that is perpendicular to the cylinder axis. We apply a shear offset to establish an initial aperture. We introduce water such that it may flow radially through the fracture aperture, and we measure the aperture change, fracture permeability, and effluent chemistry. In this system, we perform extended duration tests on geothermally relevant rock types to assess changes in permeability of sheared induced extensile fractures under conditions relevant to EGS (effective fracture normal stress up to several tens of MPa, temperature up to 250°C). Our samples are from Stripa, (Sweden), Brady Hot Springs (NV), and Desert Peak (NV) and include a granite, a meta-mudstone-volcanic from beneath 4800 feet, a rhyolite sample from beneath 3590 feet, and silicified rhyolite tuff from beneath 2476 feet.

Before and after the tests we characterize our rock mineralogy and mechanical properties (from P and S-wave velocities), and measure the surface profile of both surfaces. We assemble the fracture with a slight angular offset about the core axis, to provide an initial aperture. After making a series of system measurements, we apply our desired normal stress, raise the temperature, and flow water. Opening the fracture allows characterization of changes and the spatial distribution with respect to initial aperture. A rich suite of data has been collected.

Geomechanical modeling using TREACTMECH, and THMC modeling using TOUGHREACT are being performed to improve our overall understanding of the coupled chemical-mechanical-hydrological processes. Our modeling efforts include modeling artificial aperture fields and those derived from the experiments.

1. INTRODUCTION

Permeability in fractures is a function of aperture distribution. Apertures resulting from shear offsets can result in significant permeability, but the life-span of the aperture depends upon the fate of self-propping asperities. Asperity contacts are controlled by local chemical and mechanical conditions in the fracture. These are functions of temperature, pressure and chemical dissolution, precipitation, and mechanical deformation. As the importance of fracture flow is recognized across fields, studies on the evolution of the fracture pore space geometry are being performed (e.g. Ameli et al. 2013, Elkhoury et al. 2013, Noiriel et al. 2013, Deng et al. 2016). Conditions relevant to enhanced geothermal systems add significant complexity in making measurements, and the use of natural heterogeneous rock samples relevant to geothermal energy extraction complicate mineralogy and chemistry. Few studies conducted on the evolution of the fracture pore space geometry and resulting changes in the permeability have been performed under EGS conditions.

Ultimately, we would like to understand the dependence of different rock types, mineral compositions, stress conditions, and fracture surface textures on the longevity of fracture apertures, so that if possible, selection of reservoir rock can be optimized to reduce or eliminate refracturing where different lithologies are available. Induced fracture permeability is influenced by dilation, wear and brecciation of the wall rock, healing by mineral dissolution, grain size, and mineral replacement (Fetterman and Davatzes, 2011, Roth et al. 2013). In sheared fractures dilation results in enhanced permeability (Chen et al, 2000, Fetterman and Davatzes, 2011), and this permeability may also be anisotropic (Auradou et al, 2006, Gentier, 1997, Nemoto et al, 2007). Healed fractures containing silica or calcite that are reactivated by shear tend to undergo brittle dilation, enhancing permeability. In fractures containing minerals such as chlorite and smectite, debris/grain rotation may occur reducing dilation during shear. Such ductile deformation may result in less permeability enhancement upon fracturing. Reduced permeability may also occur because of clogged pore space (Davatzes and Hickman, 2010).

Aperture changes resulting from dissolution and precipitation strongly impact long-term performance of a geothermal reservoir. The rates of these reactions are enhanced due to the elevated temperature and circulation of fluid. In room temperature experiments, Polak et al. (2004) observed slow permeability reductions in a limestone fracture subjected to groundwater flow in a long-term [900 hours (38 days)] test. The test continued by flowing distilled water for over 600 hours. The aggressive distilled water initially caused greater

permeability reduction than the groundwater, however after some time, the permeability increased quickly because of the formation of wormholes. In fractured novaculite in an experiment lasting over 900 hours over a range of temperatures up to 150˚C, Polak et al. (2003) observed reductions of the hydraulic aperture by a factor of 6. Smooth decreases in hydraulic aperture were interspersed with rapid decreases attributed primarily to breaking asperities under increased effective stress. In modeling the tests, Yasuhara et al. (2004) considered the effect of pressure solution resulting in dissolution of the asperities.

The importance of the fracture asperity-fluid interaction, particularly when asperities are subjected to elevated stress is shown in these and other studies. How permeability in rock fractures changes over time and correlations between specific rock types/mineral constituents and have not been well established. Long-duration laboratory fracture flow tests on a series of rock samples are required to better understand these correlations. Because the very large number of conditions (mineralogy, temperature, water chemistry, stress) under which the permeability of fractures is important, select laboratory tests are needed to provide data useful in building confidence in numerical modeling. Predicting how fractures in different rock types will evolve under a variety of pressure-temperature-composition conditions, altering existing and induced permeability, is a benefit that could allow operators strategies to select regions that contain rock types that are more amenable to maintaining their fracture permeability under natural or applied conditions, thus reducing refracturing costs at later times.

We have performed a series of tests examining permeabilty changes in fractured geothermally relevant rock under EGS conditions and have modeled a number of the tests. Our tests were performed in a custom experimental system that induced water flow through the fractures, and allowed measurements of fracture aperture change, permeability change, and effluent water chemistry. We briefly present results of four tests here, one using Stripa granite, the other using core samples from the Brady and Desert Peak geothermal fields. We relate our observed permeability changes by assuming two model geometries: parallel flat fractures, and cylindrical wormholes. In our tests, the hydraulic aperture was very strongly influenced by the system mechanical loading, and longer-term changes were likely the result of geochemistry.

2. EXPERIMENTAL STUDY

Four rock types were included in our experimental investigation – granite, dense metasediment, rhyolite tuff, and a silicified rhyolite tuff. Our tests were conducted in a unique custom test apparatus. The apparatus and tests are described below.

2.1 Description of initial core samples

Core samples from geothermally relevant rock types were selected for the hydrothermal experiments. These included a granite and three samples from Ormat; two from the Brady BCH-03 well, and one from the Desert Peak DP 35-13 well. The BCH-03 well is located very near the Brady 15-12 well, which was the subject of a DOE-funded EGS field well stimulation project. A multi-stage hydraulic stimulation program was conducted in the bottom 800 feet of the 15-12 well, but no sustained enhancement of the permeability has been achieved to date.

Our **granite** sample was obtained from the Stripa mine in Sweden. Petrographic analysis of this sample (Fig. 1 top left) reveals the presence of microcline (identified by crosshatch twinning), quartz (with undulatory extinction), plagioclase, and muscovite. The granite has some alteration, with a fine-grained quartz vein cutting through the sample. A published description of this granite reports the following range of mineral abundances: quartz: 35-45%, plagioclase (partially seriticized): 35-39%, microcline: 12-24%, with minor amounts of chlorite, muscovite, biotite, and epidote (Olkiewicz et al., 1979). Figure 2 (top left) shows the approximate spatial density distribution for the granite sample with the density histogram on the right.

The two samples from the BCH-03 well were selected to represent distinct lithologies. The deepest sample is a **meta-sedimentary mudstone** from 4873.0-4873.7 feet, corresponding with the lower stimulation zone of the Brady's EGS project. This sequence was described by Lutz et al. (2011) as consisting of highly deformed to foliated fine-grained metasedimentary rocks with abundant chlorite. Petrographic examination of this sample (Figs. 1 and 2 top right) indicates that it is a fine-grained, highly altered metasediment cut by a calcite vein. Small quartz grains have undulatory extinction, and the groundmass is altered to clay and calcite. A correlative sample (DEP11) from a depth of 4863.0-4863.4 feet analyzed by TerraTek (2011) is described as a fine-grained, highly chloritic meta-mudstone with 55-61% total clay and well-defined clayey foliation planes and a sheared fabric. Figure 2 (top right) shows the approximate spatial density distribution for this sample, with the density histogram on the right.

A second sample of the BCH-03 core used in the hydrothermal experiments was a **rhyolite ash flow tuff** collected from a depth of 3944.5 to 3945 feet. This is part of a sequence of devitrified rhyolite ash flow tuffs that are present from 3,700 feet to about 4,100 feet in the BCH-03 well (Lutz et al., 2011). Petrographic examination of a thin section from 3944.8 feet indicates that it is a crystal-rich rhyolite tuff with phenocrysts of plagioclase, quartz, biotite, and iron oxides (Figs. 1and 2 bottom right). A correlative sample (DEP4) from a depth of 3899.0-3899.4 was described by TerraTek (2011) as a devitrified rhyolite with less than 21% quartz and less than 21% total clay. XRD and QEM-SEM analyses reported by Ayling et al. (2012) for a similar rhyolite ash flow tuff sample from a depth of 3902 feet reported the following mineral abundances (QEMSCAN values listed in parentheses): quartz – 9.5 (2.5)%, micas – 5.3 (5.8)%, calcite – 14 (12)%, alkali feldspar – 6.9 (6.3)%, plagioclase – 43 (46)%, smectite and chlorite – 13 (14)%, and illite – 1.5 (1.1)%. Other detected phases (present in minor abundance) included pyroxene, zeolites, oxides, and dolomite. Figure 2 (bottom left) shows the approximate spatial density distribution for this sample, with the density histogram on the right.

The shallowest sample studied, from the DP 35-13 core from the Desert Peak geothermal field, is a **silicified rhyolite tuff** sample from 2476.2 to 2477 feet. This sample is part of a sequence of Tertiary ash flow tuffs described by Lutz et al. (2010). Petrographic examination of this sample via thin section revealed the presence of 3-4 mm blocky plagioclase and sanidine crystals and a population

of smaller subrounded crystals of feldspar and quartz in a fine-grained groundmass, with clay and calcite observed as alteration phases. TerraTek (2009) described a correlative sample from a nearby depth of 2483.6 feet as a siliceous rhyodacite to rhyolite ash flow tuff with phenocrysts of plagioclase, quartz, and sanidine in a densely welded, devitrified, and silicified groundmass that contains quartz and potassium feldspar along with alteration phases illite-smectite, kaolinite, chlorite, and calcite. XRD analysis of a sample from 2484 feet from this same well yielded the following mineral abundances: 40% quartz, 23% potassium feldspar, 13% plagioclase, 8% illite/smectite, 5% kaolinite, 3% chlorite, 2% illite and mica, 1% calcite, 2% dolomite, 2% hematite, and 1% anatase.

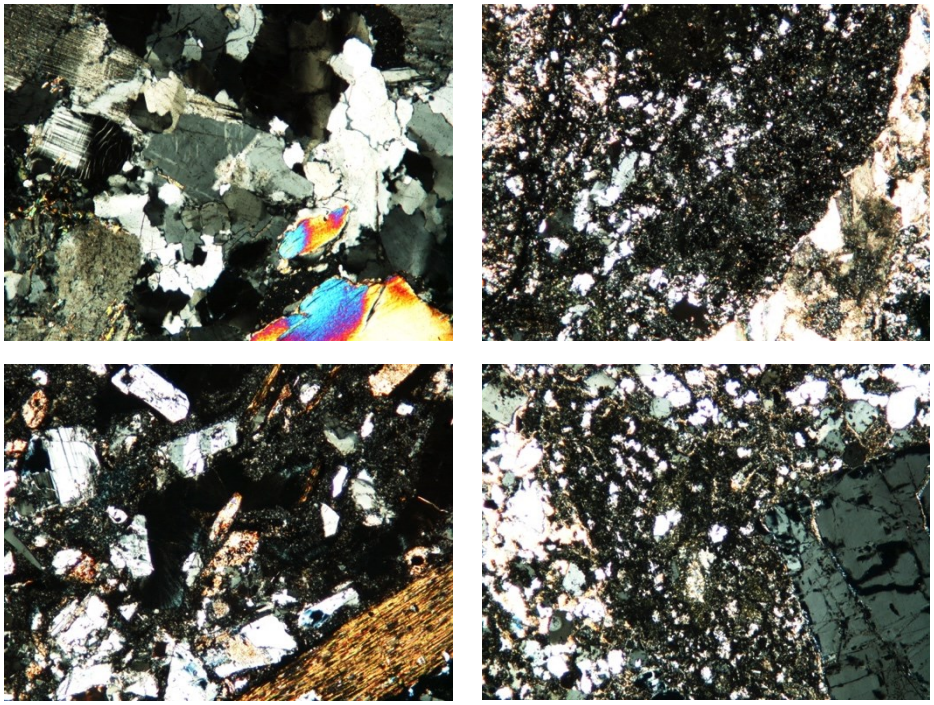

Figure 1. Top left - photomicrograph of Stripa granite under crossed nicols; top right - photomicrograph of BCH-03 meta-sedimentary mudstone from 4873.2 feet under crossed nicols. Calcite vein cuts sample on the right side. Bottom left - photomicrograph of BCH-03 rhyolite ash flow tuff from 3944.8 feet under crossed nicols; bottom right - photomicrograph of silicified rhyolite tuff from DP 35-13 well from 2476.2 feet under crossed nicols. Bottom side of photos is 1.75 mm.

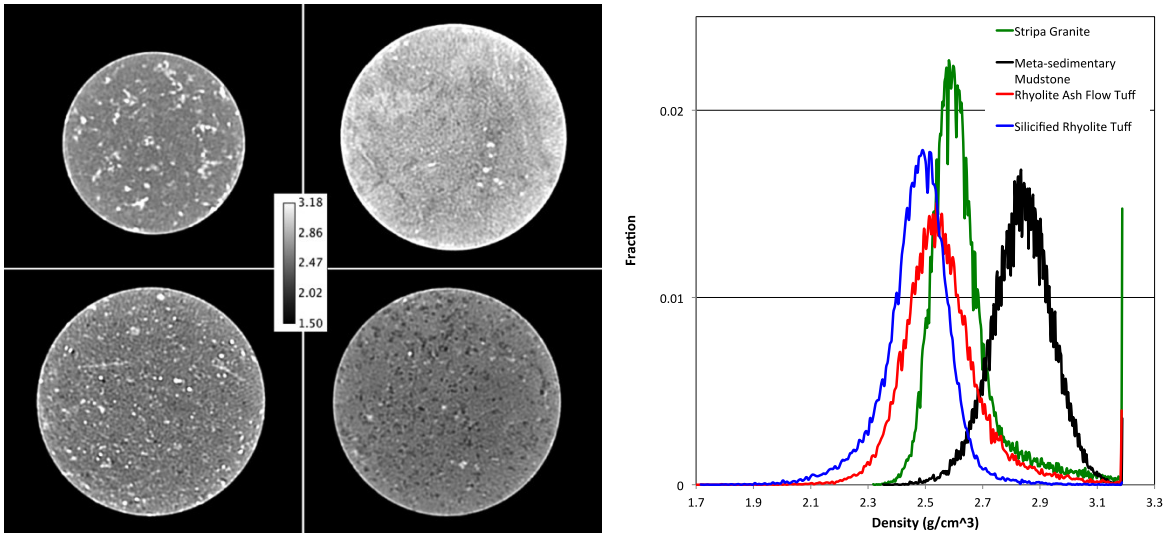

Figure 2. X-ray CT cross sections showing approximate density distributions in samples tested. Top left - Stripa granite sample; top right - BCH-03 meta-sedimentary mudstone from 4873.2; lower left - BCH-03 rhyolite ash flow tuff from 3944.8 feet; lower right - DP 35-13 silicified rhyolite tuff from 2476.2 feet. Sample diameters are about 63 mm (Stripa –top left - sample is 49 mm). right – histogram of density distributions extracted from CT data.

2.2 Rock seismic properties

Seismic velocities and the dynamic elastic moduli of the reservoir cores were determined at room dry and temperature conditions, using ultrasonic waves (source frequencies 1 MHz for P waves, 500 kHz for S waves, Table 1). The high-density/low-porosity meta-sedimentary mudstone samples exhibited much higher seismic velocities and moduli as well as high Poisson ratio (~0.25). In contrast, other rocks showed much smaller velocities, with the elastic moduli less than half of the mudstone samples. Silicified rhyolite tuff samples exhibited very strong ultrasonic wave scattering and large attenuation, with Sample 2 being much more heterogeneous than Sample 1.

Table 1. Rock properties.

Name	Density (g/cc)	Vp (m/s)	Vs (m/s)	Poisson Ratio	G (GPa)	E (GPa)
Meta-sedimentary mudstone 1	2.7822	5577.9	3205.4	0.25345	28.586	71.663
Meta-sedimentary mudstone 2	2.7750	5590.1	3221.7	0.25134	28.803	72.084
Rhyolite ash flow tuff 1	2.3544	3778.3	2348.0	0.18540	12.980	30.774
Rhyolite ash flow tuff 2	2.3494	3694.0	2286.6	0.18939	12.284	29.221
Silicified rhyolite tuff 1	2.2867	3907.8	2317.4	0.22880	12.280	30.179
Silicified rhyolite tuff 2	2.2468	3375.5	2034.6	0.21470	9.3004	22.594

2.3 Test apparatus

Our custom test apparatus is shown schematically in Figure 3. This apparatus allows application of a normal stress to a rock core fractured perpendicularly to the rock central axis. Samples up to 5.7 cm in diameter and approximately 5 cm in length can be placed in the chamber. Prior to testing, rock cores are fractured using a custom tool that applies a compressive stress around the circumference at the center of the core, resulting in a tensile fracture perpendicular to the core axis. This fracture is strongly impacted by heterogeneities, the grain of the rock, and by the locations where load is applied, and our samples had strong variability in heterogeneity and grain. To allow water flow into the fracture, a small diameter hole is drilled along the rock central axis about 60% through the rock prior to fracturing. This allows water to flow into the center of the fracture aperture after the rock cylinder is fractured.

The details of our custom apparatus are presented in Kneafsey et al. (2015) and summarized here with additional details added. The custom pressure vessel was made from Grade 5 titanium that was cleaned and passivated to hinder corrosion and reduce contamination of water samples. In spite of this, aluminum levels in the produced water were high, possibly as a result of leaching as Grade 5 titanium contains about 6% aluminum. Most of the titanium/water contact occurs after the water flows through the sample. Graphite and Kalrez seals can be used at the top and bottom seals as a result of custom machining. Both types were used at the lower seal in different tests to allow the shaft to move vertically. Neither seal type behaved ideally, with the graphite allowing very small leaks (compare to the 0.01 mL/min flow rate), and the Kalrez decomposed resulting in local concentrations of hydrofluoric acid that caused some vessel corrosion. In the vessel, the sample rests on the titanium pedestal support, which rests on a shaft that extends through a seal in the bottom and is supported on a hydraulic jack allowing application of a normal stress on the fracture surfaces. An Active Sensors LT0951-010 high-temperature linear voltage differential transducer (LVDT) is connected to the shaft to indicate sample displacement caused by the fracture closing.

Upstream and downstream pressures (PX-1004, current versions by Omegadyne) and the pressure differential (Rosemount 1151) between the inlet and outlet are independently measured. In spite of calibration, some zero shift remains in the differential pressure measurements. This shift was measured frequently using a bypass manifold that allows isolation and equilibration of the pressure transducers, and allows independent checks of the upstream and downstream pressure transducers. The pressure transducers are maintained away from the heated portion of the test at room temperature. Room temperature affected the differential pressure measurements (~0.007 psi/C) but room temperature was fairly stable over the course of the tests. The differential pressure transducer is set to indicate differential pressures up to about 100 kPa. Pressure differentials in excess of this value are calculated using the upstream and downstream pressure transducers.

Flow to the sample is provided using a high-pressure syringe pump (Teledyne ISCO 500D). Flow to the sample passes through a temperature equalizer bath and then to the vessel and sample to ensure that the inlet (and outlet) tubing are kept cool. Water entering the sample first flows through the cylindrical hole in the top half of the sample to the fracture, where flow resistance is governed by pressure and aperture geometry. The flow rate used was 0.01 mL/min with the exception of startup measurements. At that rate, water is heated as it moves through the pressure vessel top, and no pre-heating is used. We used distilled deionized water. After passing through the fracture, water is collected at the outer radius and flows out of the vessel, through the temperature equalizer bath, through a back-pressure regulator (Equilibar) controlled by another high-pressure syringe pump (Teledyne ISCO 500D), and is collected in aliquots using a fraction collector (GE Healthcare). We performed our tests at a fluid pressure of 10.3 MPa to maintain water in the liquid state at all of our experiment temperatures.

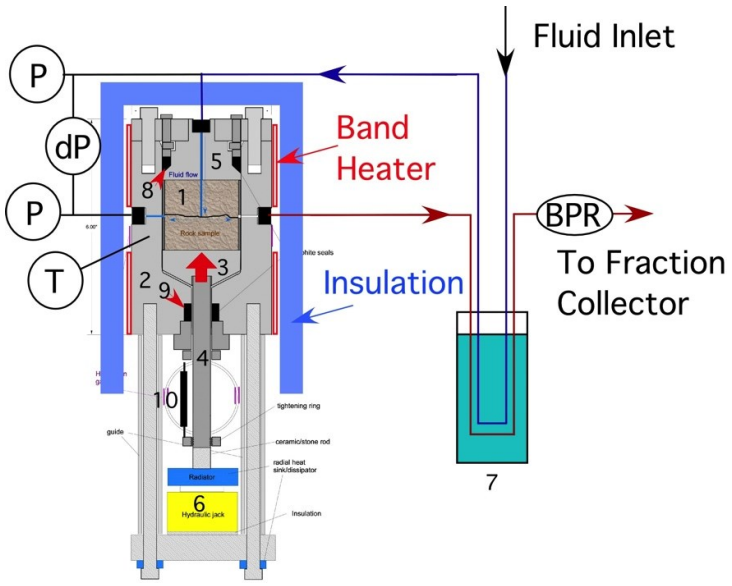

Figure 3. Experimental apparatus schematic. 1. Fractured rock sample, 2. Pressure vessel, 3. Platform, 4. Shaft, 5. Top, 6. Hydraulic jack, 7. Temperature equalizer bath, 8. Top seal, 9. Bottom seal, 10. LVDT

2.4 Room temperature rock/fracture mechanical behavior

Prior to heating the sample, initial fracture closure and permeability changes were measured as effective stress was increased (Figure 4). The initial closure of the sheared (rotated) fracture in the rock cores was measured as a function of the effective stress on the fracture. Pore pressure (10.3 MPa, 1,500 psi) was applied to the samples under room temperature, and then the effective stress was increased stepwise up to 20.7 MPa (3,000 psi). The mean apertures shown in Figure 4 were calculated by subtracting the measured closing displacement of the fractures from the aperture of unloaded fractures measured before the core samples were introduced in the test cell. Note that the final data point in each plot indicates the aperture after the test cell temperature was increased up to 250°C while maintaining the effective stress.

The initial aperture of the fracture in Stripa sample was smaller than other cores. Also, the rotation of the sample was not prohibited (no alignment pin was used to prevent the sliding of the fracture surface back to the mated state). The unusual convex shape of the aperture-stress curve indicates that the deformation was not elastic (the fracture softens with increasing stress), and possibly, the fracture surface was sliding resulting in a decrease in aperture.

Possibly because of smaller initial rotation angle compared to the other samples, the silicified rhyolite tuff sample had smaller initial and final apertures. Note that the rhyolite ash tuff sample was loaded twice within an interval of ~1 month. This is because the sample was prematurely unloaded after ~1 week (Test 1), and the sample had to be reintroduced in the test cell after making repairs to the test apparatus. Possibly for this reason, the overall reduction of the fracture aperture was the largest, and the compaction during the second loading was much smaller than the other tests.

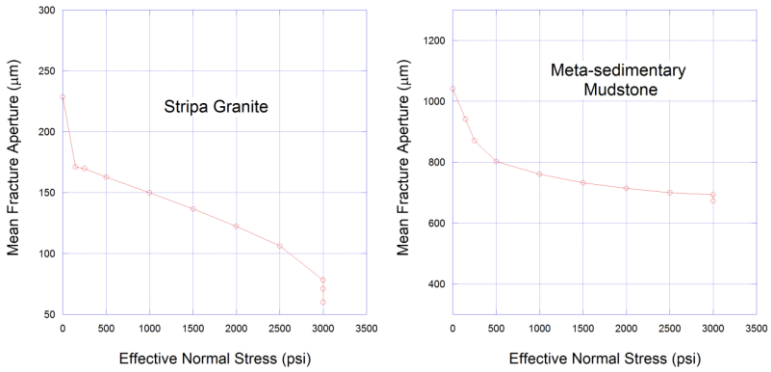

a. b.

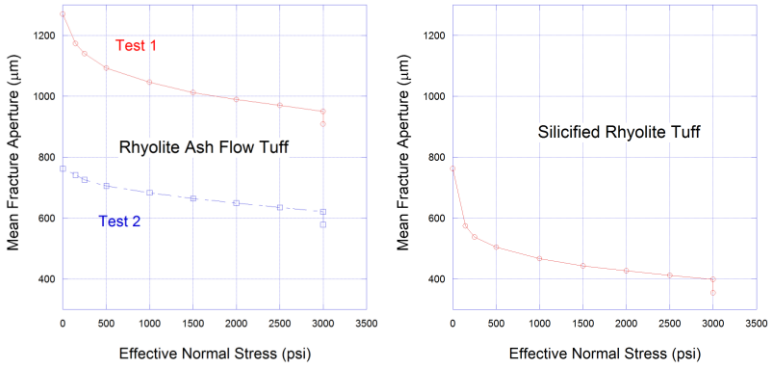

c. d.

Figure 4. Initial fracture closure under uniaxial loading. The pore pressure was 10.3 MPa (1,500psi), and the temperature was room temperature (except for the last data point at effective stress 20.6 MPa (3,000psi) and experiment temperature). The silicified rhyolite tuff sample (d.) had the smallest initial fracture aperture, and also exhibited a large compaction. The rhyolite ash flow tuff sample was loaded twice because of an interruption of the experiment after the first week (c).

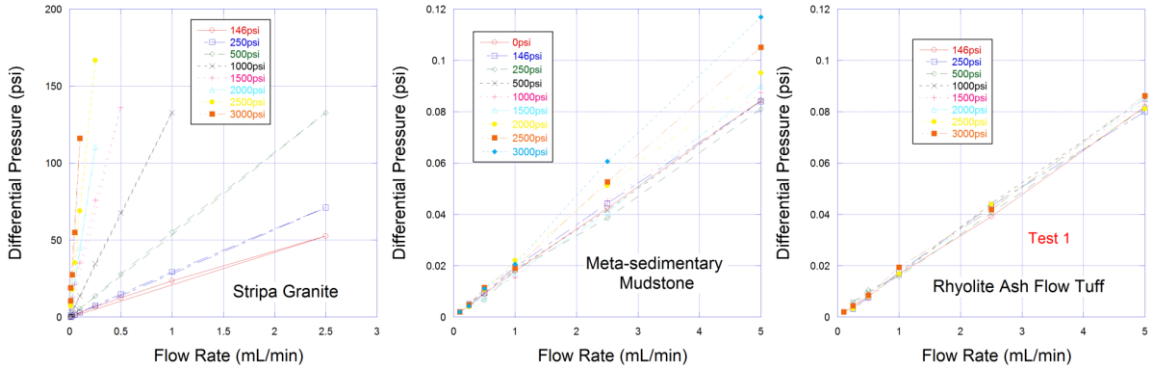

a. b. c.

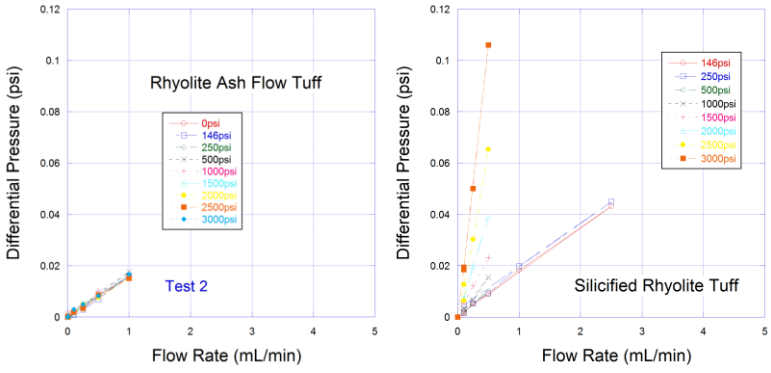

d. e.

Figure 5. Hydraulic transmissivity measurements of unheated fractures under varied effective stress. For reference, 200 psi is 1.38 MPa, and 0.12 psi is 827 Pa.

During the step loading of the fractures, radial flow was introduced in the fracture to determine its hydraulic transmissivity as a function of the effective stress. This was done by applying the fluid flow at a constant rate and measuring the resulting differential pressure between upstream and downstream pressure measurement points, for a range of flow rates and effective stresses (Figures 5 and 6). Although this setup is ideal for determining the permeability of low-permeability fractures, accurate measurement of the fracture transmissivity for small flow rates and large fracture apertures is imprecise because of comparatively large flow resistance in the system. For meta-sedimentary mudstone, reliable data were obtained only for relatively large effective stress (>~10 MPa) and high flow rate of 5 mL/min. For the rhyolite ash flow tuff samples, the transmissivity was too high (estimated to be higher than 10^{-11} m^3) and the resulting pressure drop across the fracture was exceeded by the system flow resistance. In contrast, the silicified rhyolite tuff exhibited

significantly large changes in differential pressure, which allowed us to capture the large drop in the fracture transmissivity (from ~10^{-11} m^3down to 2.2-2.3 x 10^{-13} m^3) for a wide range of flow rates and effective stresses. Because of the very small fracture aperture, the Stripa sample exhibited very small transmissivities.

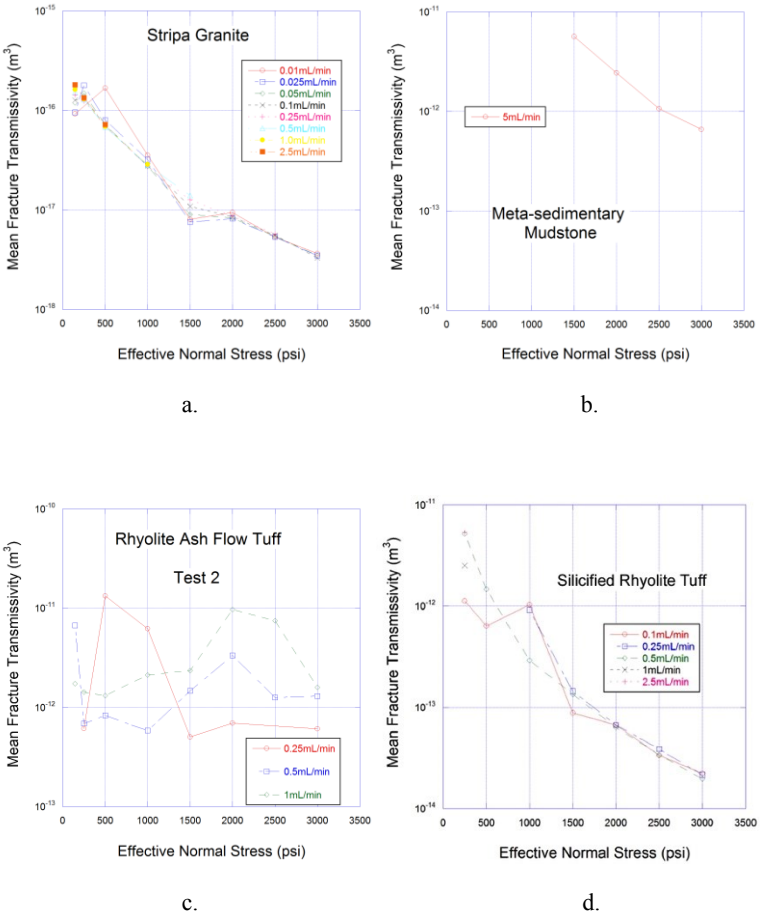

Figure 6. Fracture transmissivity with increasing effective stress for fractures in Stripa granite, meta-sedimentary mudstone, rhyolitic tuff, and silicified rhyolite tuff samples.

2.5 Test Procedure

The rock was machined to specific tolerances by D. K. Milovic Company (Livermore CA). After preparing the rock sample (machining, drilling, and fracturing), a titanium ring machined with an interference fit is heated, placed over a sample half, and cooled. The outer diameter of the titanium ring fits in the vessel with a close tolerance to minimize dead volume. Holes in the ring allow for placement of pins to help maintain the intended rotational misalignment of the two fracture halves. A profilometer (Nanovea PS-50) is used to describe the fracture surfaces. The travel on the scanning table is less than the diameter of the cores we are using. To accommodate for this and allow the entire surface to be scanned, a second stage is fit to the original stage allowing sample placement in four relatively precise locations reducing (not eliminating) data stitching and registering. Upon completion of the profiling, photographing, and observation, the two samples are matched, and then an angular offset is applied and held in place using the pin. The sample is carefully installed into the vessel, and the vessel is assembled and connected to the flow system. Two 1/8 inch thick copper plates, formed to match the outer diameter of the vessel and the inner diameter of the heaters are placed around the vessel to enhance heat distribution, and the heaters and insulation are installed.

3. RESULTS

3.1 Pressure, Temperature, and Displacement

Pressure, temperature, differential pressure, displacement, and computed planar aperture and wormhole dimensions are presented in Figure 6 (Kneafsey et al., 2016) and summarized here.

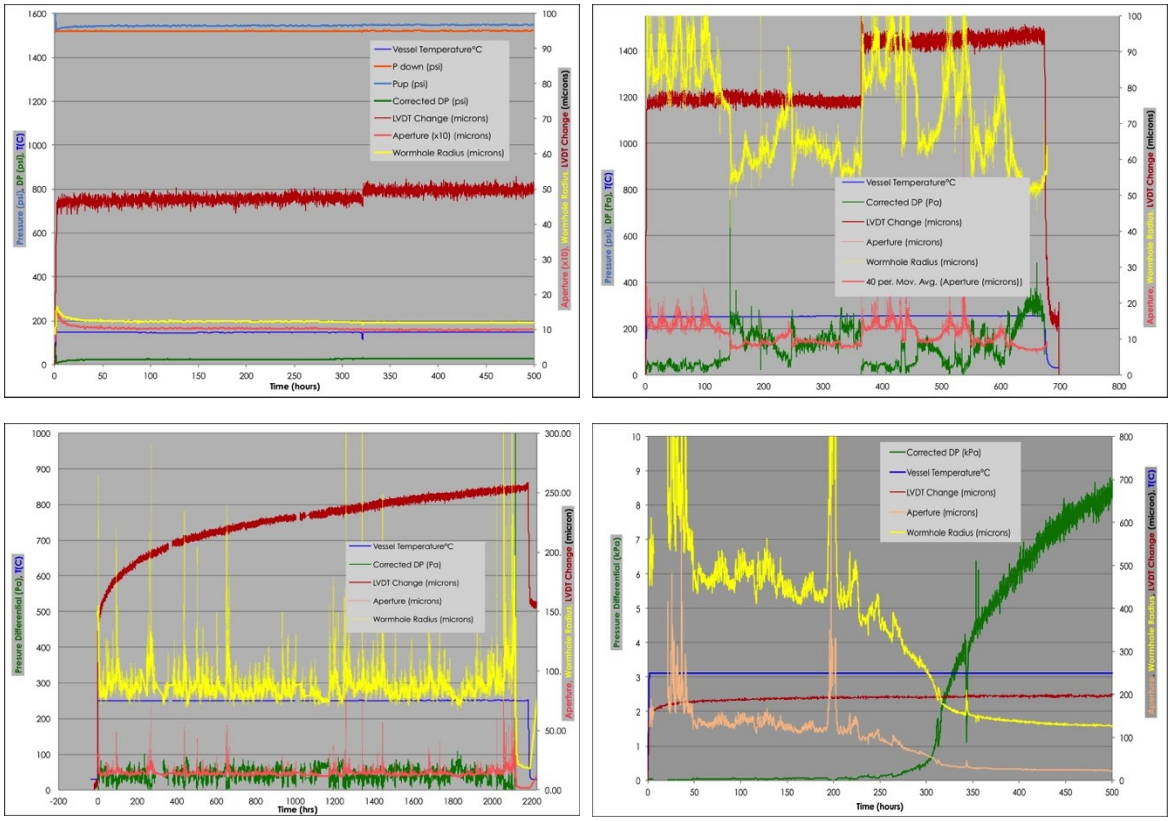

Figure 7. Pressure, temperature, differential pressure, displacement, and computed planar aperture and wormhole dimensions upper left – Stripa; upper right – metasediment, lower left – rhyolite ash flow tuff, lower right – silicified rhyolite tuff. Note the line colors and the axis labels are correlated.

The Stripa test was performed at 150°C, whereas the other tests were performed at 250°C. In each of the panels in Figure 7, the green curve represents the pressure differential across the sample. These data along with properties of water at the experiment conditions are used to compute the permeability and dimensions of a fictitious planar aperture and wormhole, two end members that could describe a fracture (see Kneafsey et al, 2015 for details). Differential pressure measurement error and noise are compounded significantly (to the third and fourth power) in the computation of aperture or wormhole radius. Consequently, this is a very important measurement. Because the range of differential pressures that will be experienced in a test is not known a priori, an industrial (difficult to break) differential pressure transmitter allowing re-ranging by a factor of six was used. The transmitter was re-ranged to its lowest range, but experiment, system, and transmitter noise are evident in the plots. Corrections are needed for the value the transducer reads at zero differential, and for the difference in mass of the water on either side of the differential pressure transducer due to one side having a heated (lighter) water column. As an example, for the case of the rhyolite tuff sample in the lower left panel of Figure 6, the differential pressure was very low in agreement with Figure 5c, indicating a large aperture over several thousand hours.

The red curve in each panel of Figure 6 depicts the macroscopic closing of the fracture indicated by the LVDT. Larger positive changes indicate the sample (aperture) is becoming smaller. For the dense Stripa granite and metasedimentary rock shown in the top two panels of Figure 6, very little change in sample size occurred, with the exception of a stop-start incident in each. Each of these showed a compaction of a few microns. The Stripa sample had large differential pressures over the entire course of the experiment, whereas the differential pressure in the metasedimentary rock varied in spite of the apparent LVDT-indicated stable fracture aperture. For the rhyolite ash-flow tuff and silicified rhyolite tuff shown in the bottom two panels, there is more sample compaction. In the lower left panel describing the test with the rhyolite ash-flow tuff, there is significant compaction (100 or more microns), but no change in differential pressure. This indicates that the aperture was too large to affect the measured pressure differential in spite of the compaction. Changes in the aperture were observed also showing continued elevated permeability. For the silicified rhyolite tuff, the compaction was smaller than the rhyolite case, however the impact on differential pressure indicating a significant loss in permeability is clear. No general correlation between compaction and permeability was observed. Post-test images of the bottom face of each sample are shown in Figure 8.

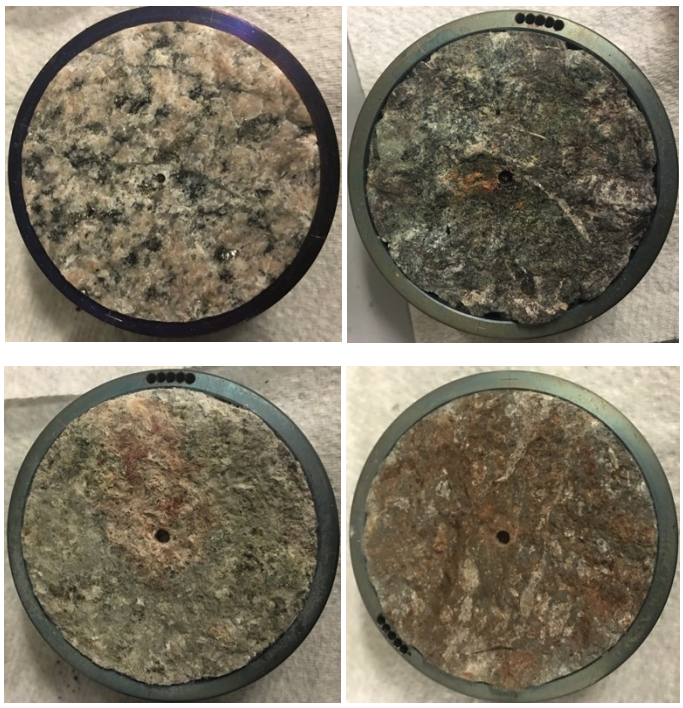

Figure 8. Photos of the bottom face of each sample. top left Stripa granite, top right meta mudstone, bottom left rhyolite tuff, bottom right silicified rhyolite tuff.

3.2 Surface profilometry and aperture calculations

Surface profiles were measured using a Nanovea PS-50 optical profiler before and after fracture sustainability testing. Data were processed using ImageJ software (Rasband, W., ImageJ 1.50e and newer, imagej.nih.gov/ij). When using the profilometer, the scan data are collected for overlapping quadrants of the rock face. Moving the stage results in four different scan heights. The data are then normalized and stacked using Matlab, and then the resulting compiled quadrant data are stitched together in ImageJ using the pairwise stitching plugin (Priebitch et al. 2009) to make a circular profile surface. The circular fracture surfaces from each face, top and bottom from pre- and post-test were registered to align them and then subsequently subtracted from each other to estimate aperture and changes to the topography of the surfaces. Numerically creating the aperture under non-stressed conditions is a non-trivial problem although it is conceptually easy. Incorporating effective stress and rock property heterogeneity adds significant difficulty to determining the resulting aperture (discussed below).

3.3 Water Chemistry

Effluent water chemistry from the tests is summarized below. Influent water was distilled and deionized, thus aggressive. Water samples were collected by an automated sample collection system (Frac-920, General Electric) that was programed to collect composite 6 hr samples under open laboratory conditions, which at the experimental flow rate of 0.01 mL/min averaged at 3.6 mL/sample. Input fluid was deionized water (MilliQ Elix, Millipore, 18 mΩ) that was analyzed independently and shown to have no detectable anions, cations, or Si (data not shown).

Cations in the effluent samples were analyzed on a Perkin Elmer Elan DRC II ICP-MS instrument after being acidified and diluted with 2% ultrapure HNO_3 acid. Ammonia gas was used as the reaction gas in the Dynamic Reaction Cell of the Elan DRC II ICP-MS instrument to remove isobaric interference from Argon carrier gas and sample matrix, especially for the analysis of Fe, Ca and K elements. A mixture of Li6, Sc, Ga, Tm and Rh solution was used to provide the internal standards and was spiked into both the calibration standards and effluent samples to correct for any potential instrument drift during sample analysis.

The anions were analyzed on a Thermofisher Dionex 2100 IC instrument equipped with an IonPac AS 11 analytical column. The analysis was performed under isocratic mode with 30mM KOH as the mobile phase at a column temperature of 30 °C. Samples were diluted 5 to 12 times with ultrapure D.I. water before being analyzed on the IC instrument.

Strict mass and charge balances were not possible for the experiments because we were not able to monitor bicarbonate due to the design of the fluid collection system. Additionally the ion concentration tended to spike early in the experiment before reaching steady state concentrations. A blank system sample was run using a Ti plug in place of the rock core, after the other rock samples were completed, and showed some contamination from Al, Si and F. The Si may have been from precipitation from previous samples in the outlet line, and the F was likely from degradation of sealant materials. Al was most likely contamination from the Grade 5 titanium (6% Al) surface. The average concentration of anions, cations and silica of all rock type tested is shown in Tables 2 and 3.

Table 2. Average cation concentration (mg/L) in each test.

	Li	B	Na	Mg	Al	K	Mn	Ca	Fe	Rb	Sr	Ba
	mg/L											
Stripa	0.03	0.14	17.1	0.08	2.23	2.15	0.01	6.83	0.01	0.01	0.03	0.11
Meta Sedimentary	0.25	0.61	90.8	0.04	9.42	2.64	0.00	0.05	1.10	0.02	0.02	0.00
Rhyolite tuff	0.41	1.07	123.8	0.02	4.73	7.52	0.00	1.51	0.02	0.04	0.03	0.00
Silicified Tuff	0.30	0.83	63.7	0.02	3.33	9.22	0.00	0.01	2.13	0.03	0.02	0.00
Blank	0.20	0.00	2.1	0.34	31.95	1.96	0.05	0.06	3.13	0.01	0.02	0.00

Table 3. Average anion and SiO_2 concentration in each test (mg/L)

	F	Cl	SO_4^{2-}	NO_3^-	PO_4^{3-}	SiO_2
	mg/L					
Stripa	0.68	4.78	1.72	0.79	0.05	20.7
Meta Sedimentary	31.43	2.76	2.43	0.00	0.00	217.4
Rhyolite tuff	23.19	113.27	2.51	0.02	0.00	162.8
Silicified Tuff	15.86	32.58	6.80	0.00	0.00	170.7
Blank	96.90	0.12	0.48	0.06	0.00	78.5

3.4 Reacted fracture surface characterization - scanning electron microscopy and energy-dispersive X-ray spectroscopy (SEM/EDS) and X-ray diffraction

Fracture surfaces following sustainability experiments all display both 1. weathering features and 2. precipitation of newly formed phases in spite of the use of DI water and the short residence time. The weathering involves mainly the plagioclases, which are compatible with andesine/labradorite chemistry, for the meta-mudstone, rhyolite ash-flow tuff, and altered silicic rhyolite tuff samples, and for the Stripa sample a more sodic composition, close to pure albite is found. Calcite, showing weathering structures, is present in the meta-mudstone sample as well. The chemistry of the plagioclase, and the availability of calcium in general, apparently seems to significantly affect the crystallization of the new phases, where in the Brady samples we observe the growth of calcium zeolites, high in aluminum, such as phillipsite and wairakite, whereas in the Stripa sample the lack of calcium available and the different general chemistry triggers the unexpected crystallization of aluminum hydroxides such as diaspore.

The identification of secondary phases has been carried out using semi-quantitative energy dispersive X-ray spectroscopy (EDS) analysis and crystal morphology observation via SEM secondary electron imaging (SE) imaging, coupled with X-ray powder diffraction (XRPD) of sample powder collected from the surface of the fractures. The identification of the different phases was rather challenging due to the small amounts of samples, crystal size, and distribution, but combination of these different approaches has allowed us to obtain reliable identification of phases setting mutual restriction of the candidate secondary phases by morphology, chemistry, and X-ray diffraction signal.

3.4.1 Stripa

Figure 9 shows SEM images highlighting dissolution and precipitation features observed as a result of the Stripa test. The dissolution of feldspar is evident in this sample, along with the crystallization of aluminum hydroxide in the form of sub-micrometer crystals of diaspore. Zeolites were not observed. No clear secondary phases containing relevant amounts of silicon were identified. Plagioclase in this sample is mostly sodic (close to pure albite), whereas andesine/labradorite are present in the Brady samples. SE images are shown, and EDS was performed on some locations to provide elemental information. As seen, significant amounts of only Al and O highlight the presence of diaspore. Albite was observed to dissolve, and diaspore crystal aggregates precipitated during the test.

3.4.2 Meta-mudstone

Figure 10 shows SE images of the post-test meta-mudstone sample. The meta-sedimentary mudstone sample shows rather complex surface features and the identification of secondary phases is very challenging due to the lack of diagnostic morphological features. EDS data show compatibility with calcium-rich aluminum-silicates. Dissolution features on reactive grains, mostly carbonates, are evident. Additional pre-existent phases are chlorite, biotite, and clays.

3.4.3 Rhyolite ash-flow tuff

The surface of the rhyolite ash-flow tuff sample shows areas where significant preferential dissolution of some grains happened. The observations of the residual and of the weathered crystals surfaces suggest that significant dissolution of plagioclase (andesine/labradorite) is the main process involved. Figure 11 shows SE images of the post-test sample.

We have identified calcium aluminum silicates as secondary phases, compatible in both chemistry and crystal morphology with phillipsite, more evidently present here than in the meta-mudstone sample. The prismatic shape with oblique termination, the presence of calcium as the main cation, and the large amount of aluminum (in addition to the crystallization conditions) suggest phillipsite (confirmed by XRPD). In addition to phillipsite, the precipitation of crusts extremely rich in iron (as oxyhydroxides) and illite/smectite crystals are observed as well.

3.4.4 Silicified rhyolite tuff

The surface features of the silicified rhyolite tuff sample are more variable and they highlight a more complicated crystallization history than other samples. Figure 12 shows SE images and EDS results from locations on the silicified rhyolite tuff sample. As with the Brady samples, the dissolution of plagioclase in this sample from Desert Peak is evident, but markedly different newly-formed phases can be found. Crystals similar to the phillipsite are observed on parts of the sample. In addition to those, new crystals with octahedral shape are present as well. Given the peculiar morphology and the chemical composition, these crystals have been identified as wairakite. Coatings rich in iron and in clays (smectite) can be found on the surface of the reacted fracture as well.

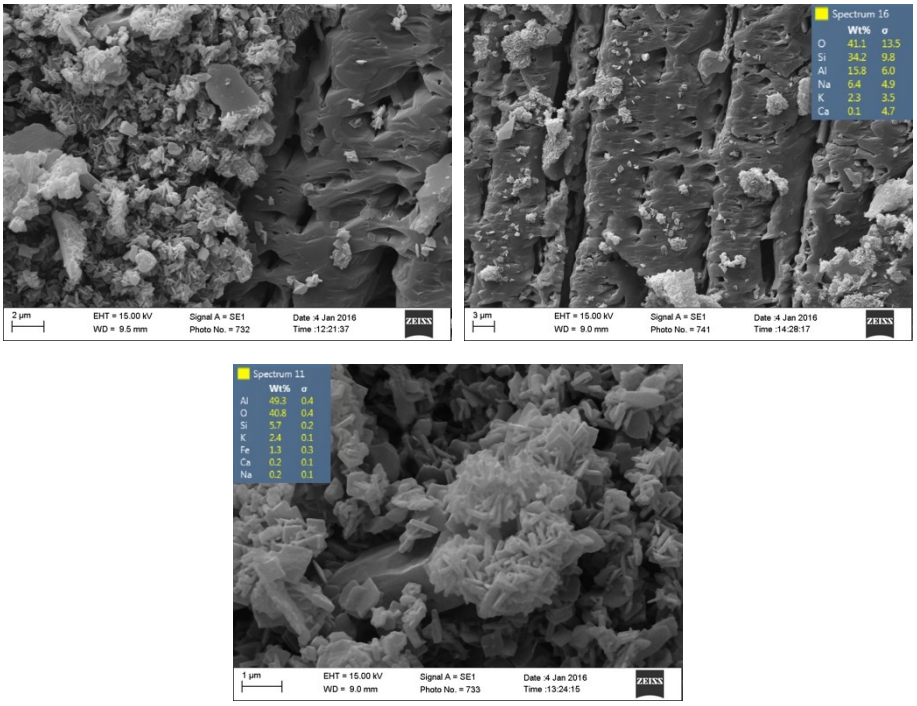

Figure 9. (Stripa granite) top left - typical Stripa sample surface featuring a weathered albite crystal (on the right) with dissolution pits, and newly crystallized diaspore rosette crystal aggregates (on the left) coating the surface; top right - SE image highlighting the dissolution pits in albite and the preferential dissolution along the boundaries of the polysynthetic twinning of the plagioclase. EDS analysis confirms a mostly sodic plagioclase; bottom - high resolution secondary electron (SE) image of the reaction products. From the EDS analysis mainly aluminum and oxygen are present. This information, coupled with the morphology of the crystals, suggests that these crystals are diaspore. No clear evidence of other phases, hosting the Na and Si derived from the dissolution of albite, has been observed.

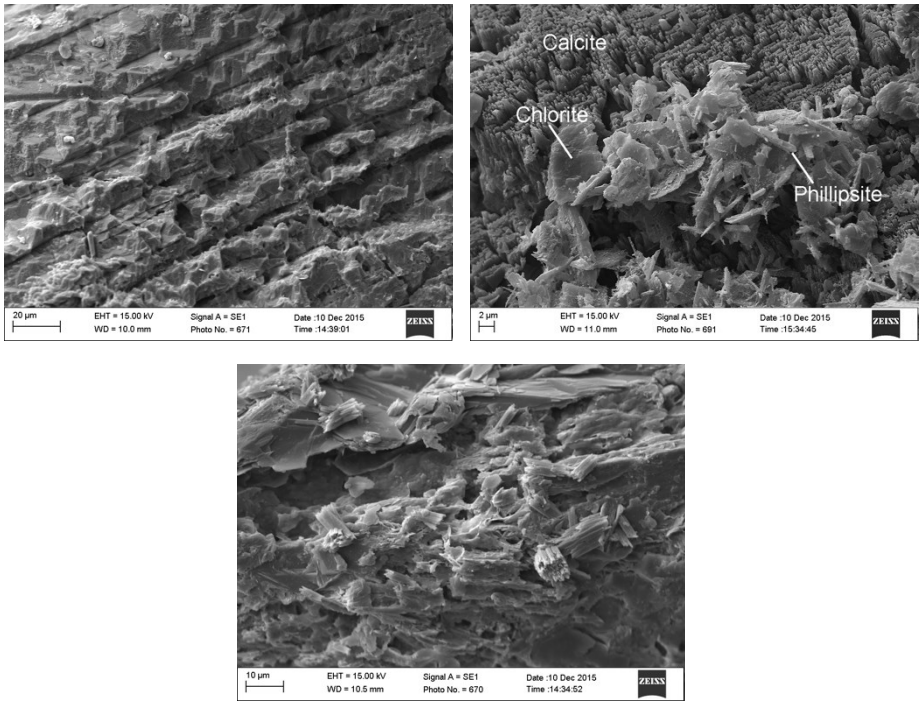

Figure 10. (meta-sedimentary mudstone) top left - SE image showing the surface of a calcite grain (identified via EDS analysis) with evident dissolution pits and enhanced dissolution along the cleavage planes of the crystal; top right - weathered calcite grain (top of image) and precipitation of secondary phase(s) (bottom of image). From the EDS analysis and the lack of clear morphological features it is not possible to give a proper identification of the new phase(s). Some platy crystals seem to be remobilized clays (e.g. chlorite), while the other precipitated material seems to be weathered mica) and a prismatic calcium aluminosilicate with a chemical composition compatible with phillipsite; bottom - thin prismatic crystals aggregates identified as apatite cover carbonates and mica grains in one part of the sample.

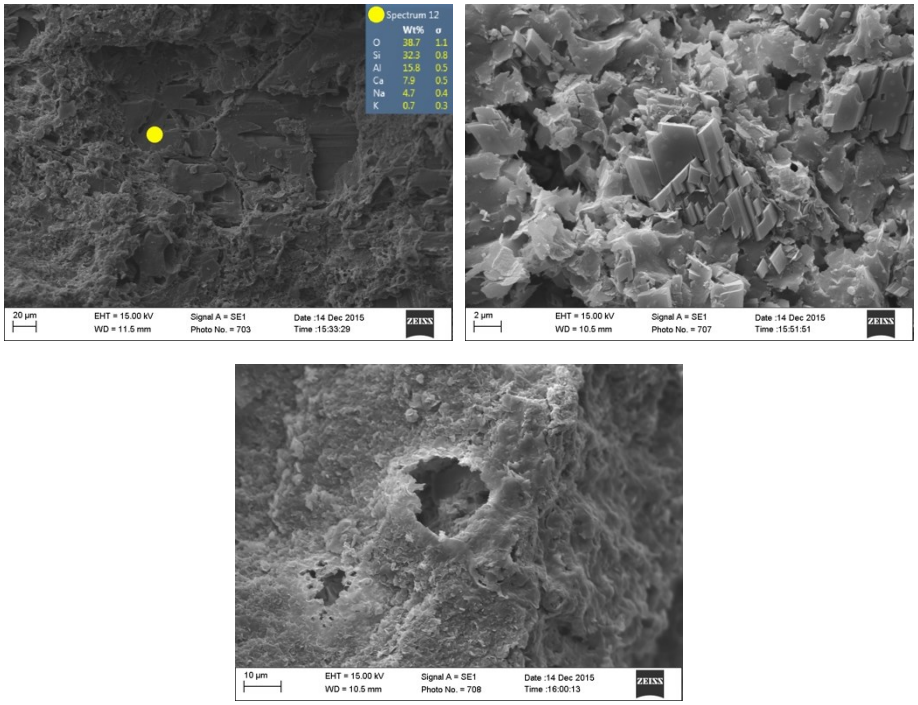

Figure 11. (rhyolite tuff) top left - SE image showing a large plagioclase crystal with dissolution features; top right - surface covered with phillipsite crystals (+ clays); bottom - example of coating of iron oxyhydroxides and clays.

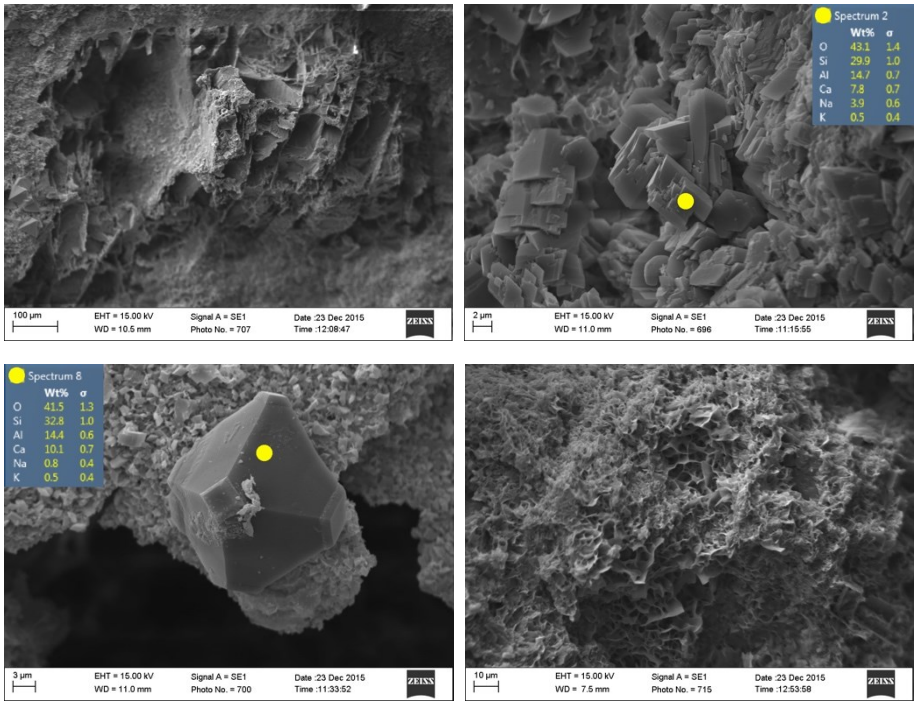

Figure 12. (silicified rhyolite tuff) top left - large crystal of plagioclase showing a high degree of weathering. The original morphology is highlighted by the residual material originally deposited in between the polysynthetic twinning lamellae; top right - part of the sample with the prismatic with monoclinic termination crystals identified as phillipsite; bottom left - example of a wairakite octahedral crystal. This crystal also highlights (overgrowth) an event that disturbed the crystallization during the experiment; bottom right - coating of illite/smectite and Fe oxyhydroxides on the surface of the fracture.

3.5 SEM/EDS examination of weathering features in post-test thin section samples

After the analysis of the morphology of the reaction products on the surface, the samples were cut vertically and thin sections prepared, including the inlet channel as well, to reveal the presence of preferential dissolution and/or chemical gradients with respect the surface of the fracture. Vertical sections are extremely efficient in highlighting weathered layers and can provide estimates about the weathering extent and mechanisms. The observations were carried out using both electron backscattering (BSE) imaging and EDS chemical maps, plus point EDS analysis to confirm the ID of the different mineral phases, when needed. Optical microscopic examination was also performed, but the results are not presented here because they do not significantly add to the SEM/EDS data.

3.5.1 Stripa granite

The weathering features in the granite sample are mostly in the plagioclase phase (Figure 13). The alteration seems to be chemo-mechanical, with the generation of a weathered surface characterized by micro-fractures. This seems to be further highlighted by the preferential dissolution of the plagioclase along the twinning planes, also confirmed by the SE observations above. The bottom BSE image, undoubtedly displaying this behavior, has been collected along the inlet. The K and Na EDS maps show the distribution of the feldspars in the sample.

3.5.2 Meta-sedimentary mudstone

The meta-sedimentary mudstone sample shows clear dissolution features, linked mostly to a specific phase, identified via EDS as quartz (Figure 14). The EDS map shows a significantly Si-depleted layer about 100 μm thick and the relative increase in Al because of the Al-rich less soluble phases are left behind. At the bottom image (a side of the inlet), fracturing and partial dissolution of two quartz grains are visible.

3.5.3 Rhyolite ash-flow tuff

A weathering layer is clearly present in this sample (Figure 15). From these thin sections, the most evident dissolution features involve calcite and quartz. The EDS map of Ca + Si displays this behavior. A closer look at the weathered layer present in the inlet (bottom BSE image) provides more detail about the weathered layer, which is heterogeneous, with a deeper dissolution of calcite and quartz (~ 200 μm), but also a thinner layer (~ 100 μm) where the other phases (mostly the feldspars) are dissolved too. The dissolution of Ca-rich phases, coupled with the availability of Si and Al in solution (dissolution of quartz, and aluminosilicates) perfectly matches with the presence of secondary Ca-rich aluminosilicate phases, such as the Ca-phillipsite identified above. The weathering of this sample involves the mobilization of Ca mostly from calcite, the Si from the quartz, and the sources of Al are likely clays and feldspars. These cations remobilized from the original rock can crystallize in the form of Ca-phillipsite, as here, or as Ca-phillipsite + Ca-wairakite, as in

the silicified rhyolite tuff. Given the presence of more reactive phases (calcite) the weathering extent of this sample is ~five times as thick as in the meta-mudstone above.

3.5.4 Silicified rhyolite tuff

Similar behavior is also present in this sample, with the BSE and EDS images showing a fast dissolution of calcite, and partially dissolved quartz grains (Figure 16). A difference with the previous samples is the apparently less homogeneous thickness of the weathered layer, likely due to the texture of the original rock, which has large phenocrysts set in a devitrified, silicified matrix.

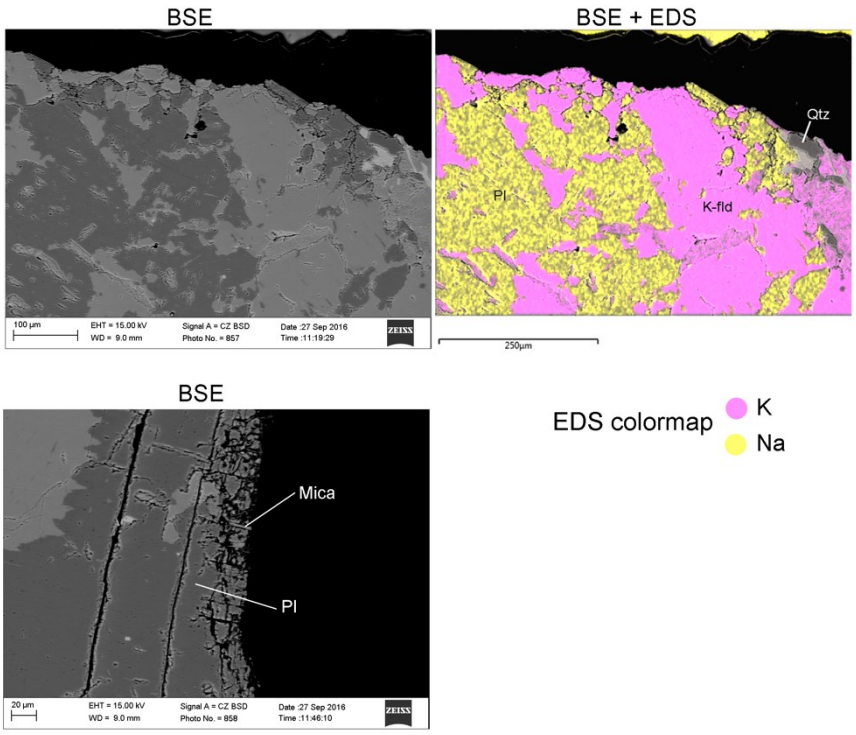

Figure 13 (Stripa granite) The BSE and corresponding overlaid image with EDS maps for K and Na highlight the presence of K-feldspar (K-fld), Na-plagioclase (Pl) and quartz (Qtz). Notice the microfractures on the first ~ 50 µm on the fracture surface. The BSE image of the inlet channel (bottom) highlights the dissolution features found in the plagioclase.

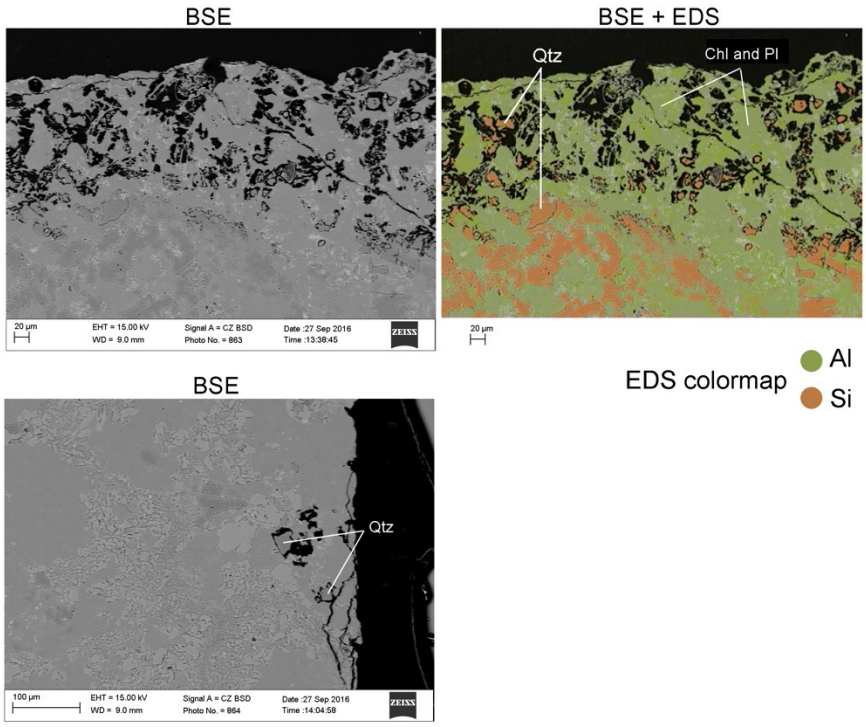

Figure 14 (meta-sedimentary mudstone) BSE and BSE/EDS figure on the top show weathered layer on the fracture surface. This layer is clearly is depleted in Si. Some relics of partially dissolved, quartz grains are visible (bright orange). The inlet channel (bottom) shows a similar behavior, to a lesser extent, and the development of larger micro-fractures.

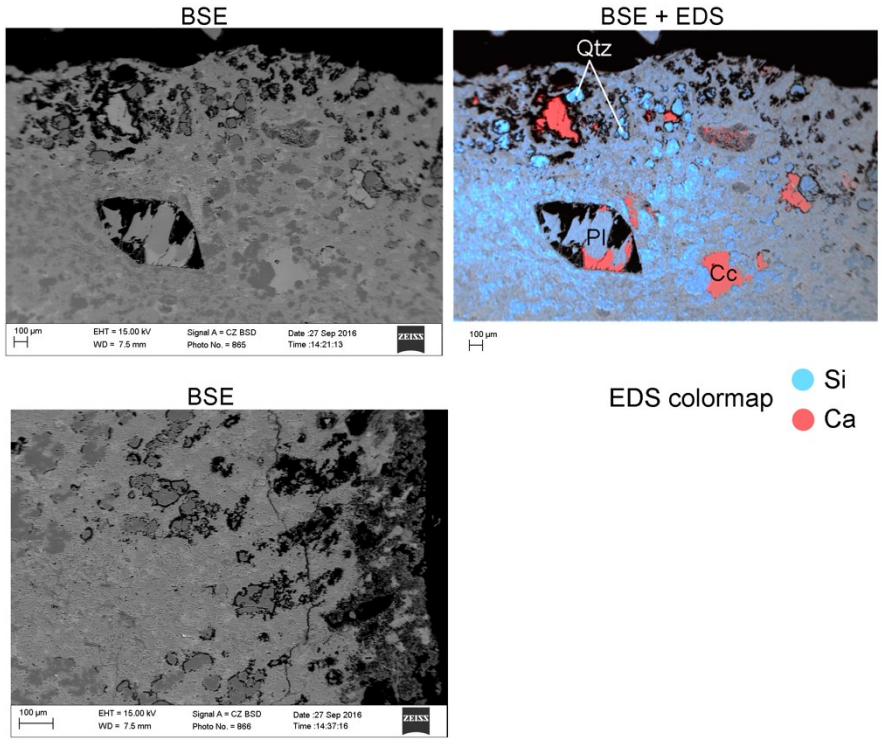

Figure 15 (rhyolite tuff) The weathering in this sample is similar to Figure 14, with the difference that calcite (highlighted by the strong signal of Ca) is also involved. Weathered layers with voids left from the dissolution of calcite and quartz are clearly visible on the fracture surface (top two figures) and the inlet channel (bottom).

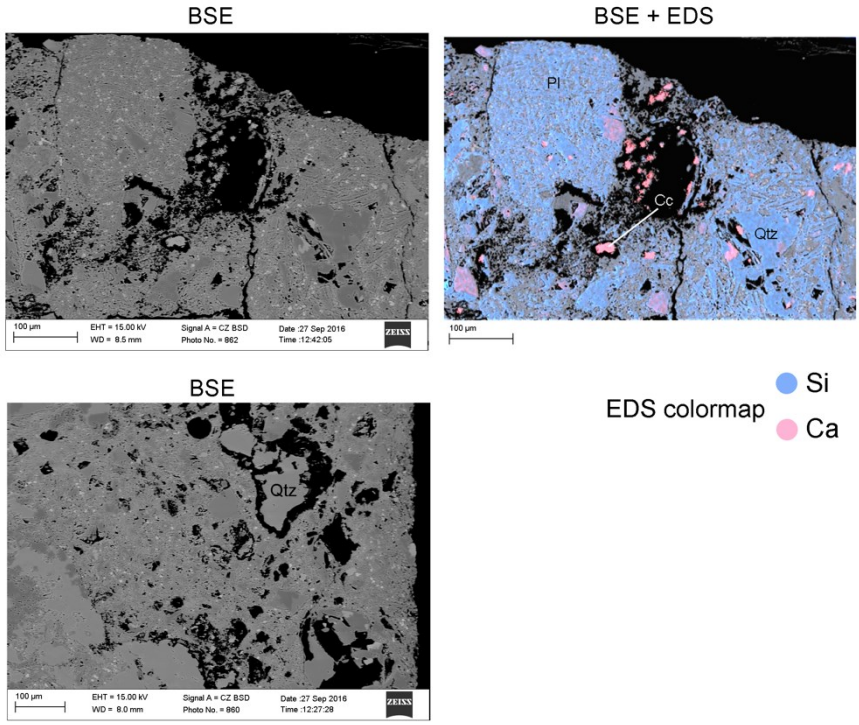

Figure 16 (silicified rhyolite tuff) The general behavior in this sample is similar to the rhyolitic tuff in Figure 15 (fast dissolution of calcite, dissolution of quartz), but the distribution of the weathering features is different due to the different texture of the sample. The plagioclase grain labeled as "Pl" is actually a textured aggregate made of mostly of plagioclase crystals.

4. GEOMECHANICAL MODELING

A geomechanical model was developed to simulate stress-induced fracture closure with an applied fluid pressure. A rhyolitic tuff sample from the 3945 foot depth of well BCH-03 at Brady's Hot Springs, Nevada was placed under 31 MPa axial stress and 10.3 MPa pore pressure at 250^{o}C. Our aim was to determine stress levels over the fracture surfaces as the initial set-up and conditions for a thermal-hydrological-mechanical-chemical (THMC) model of the experiment.

As reported in Kneafsey et al. (2016), the two fracture surfaces of the core specimen were profiled before and after the experiment. Quarter scans were overlapped allowing for offsets between quadrants, and the overlapping portions averaged (Kneafsey et al. 2016,Fig 5a,b). The half-core images were further aligned by rotating the top 8.5 degrees, which minimized the windowed mean average difference, assuming one point contact. Apertures of the oriented matched halves with three-point contact are plotted in Figure (17a). This differs from Kneafsey et al. (2016) Fig 5c in that, the core halves have been rotated into best-fit orientation and three-point contact has been assumed. In the flow experiment, the two halves were rotated, increasing their separation 450 microns from their best fit position, corresponding to a -2.4^{o} rotation of the top image. The corresponding aperture assuming a three-point contact is plotted in Figure (17b). Linear features at the edges of quadrant overlaps, are most likely artifacts in joining the profile quadrants.

Thermal-Hydrological-Mechanical modeling was performed using the new TREACTMECH simulator that combines the parallel TOUGHREACT thermal-hydrological-mechanical-chemical-biological (THMCB) code (Sonnenthal et al., 2014; Xu et al., 2011) with geomechanics (Kim et al. 2012, 2015; Smith et al., 2016).

Simulations were performed on a 36 x 36 x 12 element grid, with 0.00508 m vertical spacing through most of the grid, and 0.0108 m vertical spacing for the bottom three tiers of elements (Figure 18a). The outer-most ring of elements, and the elements making up the central hole, are given a porosity of 1.0 and water filled with a high permeability ($9x10^{-9}$ m^2), and mechanical properties 0.001 times the rock value. A second ring of elements represents the titanium alloy sleeve around the sample (114 GPa Young's modulus, 0.34 Poisson ratio, 0. porosity), with a gap between the two halves. In most layers, the sleeve is filled with rhyolitic tuff (modeled as mechanically isotropic, with 51.7 GPa Young's modulus, 0.21 Poisson ratio, 0.0345 initial porosity), except at the hole. The bottom three layers represent the apparatus piston (titanium). Mechanics boundary conditions are on components in x, y, and z directions. For mechanics calculations, the outermost ring of (water) elements are extended to the rectangle bounding the cylinder, so that mechanics boundary conditions may be applied to components normal or parallel to the exterior of the modeled domain.

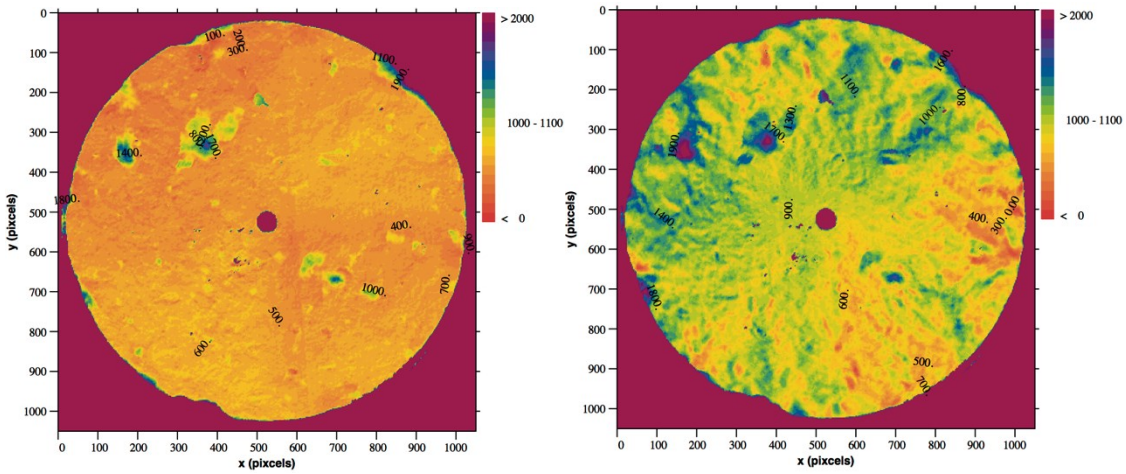

Figure 17. a) Aperture (microns) of best-fit rotation of rhyolitic tuff core halves with three-point contact. b) Aperture (microns) in experimental position -2.4° rotation, with three-point contact.

The aperture distribution shown in Figure (17b) was averaged, and a three point contact calculated. The resulting apertures are plotted in Figure (18b).

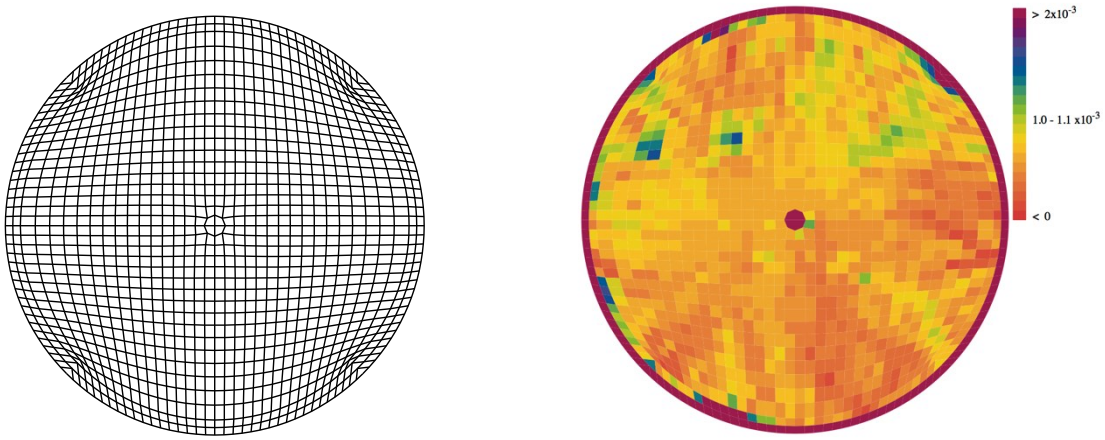

Figure 18. a) Modeling grid, plan view, 0.053 m diameter. b) Averaged aperture (m) unloaded with three-point contact.

Open fracture elements were given a porosity based on the proportion of open space and rock having a porosity of 0.0325. Initial fracture element permeabilities were calculated from the simple cubic law adding the matrix permeability (1.82×10^{-19} m^2) for the tuff fraction. Sample mechanical properties are from Lutz et al. (2011).

TREACTMECH allows modeling tensile and shear failure within elements using tangential moduli in place of original moduli in elements with open failure. Tangential moduli are the derivatives of stress with respect to strain, after accounting for the effects of failure (e.g., Borja et al., 2003). The open crack between core halves was treated as an initial open tensile failure, with an aperture scaled to give zz failure strain, and other failure strains assumed to vanish.

The simulation was started from a uniform 10.3 MPa fluid pressure and 10.3 MPa stress state (plus a small gravitational gradient) at 250 °C. This neglects constriction of the core due to the difference between thermal expansion coefficients for titanium alloy (1.11×10^{-5}/°C) and tuff (1.36×10^{-5}/°C). On the sides of the (extended) mechanics grid, elements are allowed to move parallel to the bounding surfaces, in particular, vertically, but not across the bounding surface. Fluid flow was allowed from boundary cells placed symmetrically on the outer edges of the fracture, where a constant 10.3 MPa and 250°C were maintained, with no fluid flow boundary conditions elsewhere. Water was injected into the hole at the top core. The top boundary was held at fixed z, and a uniform normal stress is applied at the bottom, initially giving 10.3 MPa average vertical stress over the sample and sleeve and ramping over 20 s to 31 MPa, and held another 20 s to allow pressures and stresses to stabilize. As vertical stress is increased, the fracture is held open initially by three elements. Strain on those elements and the surrounding rock initiates fracture closure. When the fracture closes in an element, the original unmodified elastic properties are retained, but with zero tensile strength.

Initial modeling, using tuff shear and tensile strengths based on measured unconstrained compressive strength, resulted in shear failure of the three elements containing the three contact points and elements near them, perhaps from inaccuracies in topography resultant from imperfect joining of profile quadrants. Locally, shear and tensile strengths for the tuff were increased to very high values to

prevent material failure beyond the initial tensile failure specified for fracture elements. Resultant apertures under 31 MPa average vertical stress (20.7 MPa average vertical effective stress) are plotted in Figure 19a. The fracture aperture has decreased considerably, and 25 elements are in contact. The change in aperture is plotted in Figure 19b, and varies smoothly away from elements in contact, which have less aperture change. Most of elements exhibiting less than 170 microns aperture decline are in contact, and about a third of elements with between 170 and 210 microns aperture decline are already in contact.

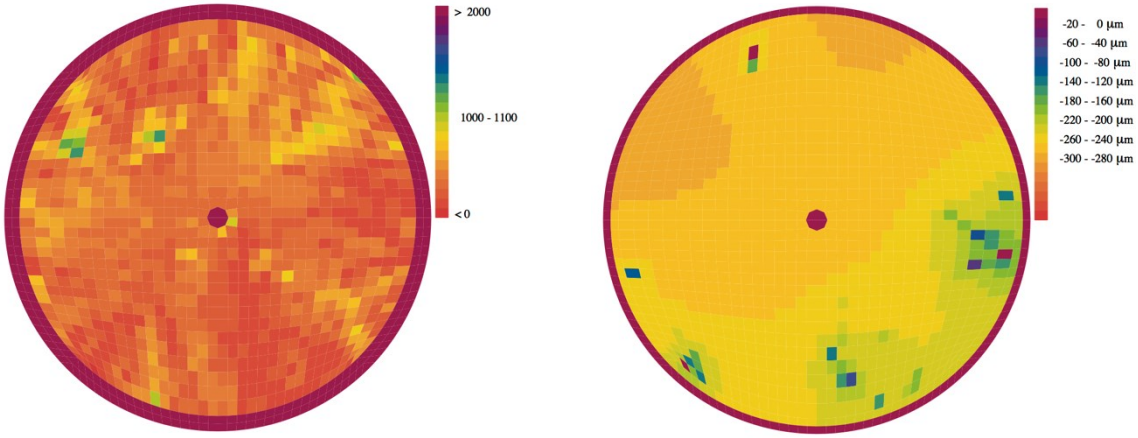

Figure 19. a) Aperture under 20.7 MPa vertical effective stress (microns). b) Change in aperture with application of 20.7 MPa vertical effective stress (microns).

To improve computational efficiency, the open crack tensile failure mechanical model of the fracture was replaced with an elastic model of the fracture. In the revised elastic model, open fracture elements were given horizontally isotropic elastic properties with vertical anisotropy. To roughly approximate differences in tangential moduli of an open tensile failure, such as fracture elements which might close with subsequent changes in local stress, the Young's modulus in the vertical direction and the Poisson ratio between horizontal and imposed vertical displacement were reduced for elements with open fracture at 31 MPa average vertical stress (i.e., with 0 aperture in Fig 19a). The fracture aperture was discretized between 0 and 200 microns inclusive truncating larger values at 200, and vertical Young's modulus and horizontal to vertical Poisson ratio reduced by a factor

$$\Gamma(\Delta) \equiv \left(\frac{\Delta_{small}}{\Delta + \Delta_{small}}\right)^{p}$$

where Δ is discretized aperture, $\Delta_{small} = 1$ micron, and $p = 1.302538$. This varies smoothly from 1 for closed fracture elements, to 0.001 for fracture elements with a 200 micron aperture or larger. That is, where the stressed gap is small, vertical moduli are close bulk values, where the stressed gap is large, the material is treated as being 1000 times more vertically compliant and 1000 times more susceptible to horizontal shear than the bulk material. Initial stresses in the revised elastic model at 31 MPa average vertical stress were set at values calculated in the open tensile failure model at 31 MPa average vertical stress.

The results of this model need to be further verified by comparing flow rates, and aperture distributions measured and calculated from the experiment. It is likely that the high stresses at contacts were relieved via grain crushing or slip. Particularly at the grain scale, some minerals are quite weak and would deform easily. This makes determining the initial geometry of the fracture once it is in place exceedingly difficult, yet of necessity to model accurately geomechanical deformation and stress-mediated reactions leading to plastic strain (eg., pressure solution creep) at the core-scale. At much larger scales in the field the fracture surface properties are only known at best on an average or statistical sense, so that modeling can capture the essential processes without having to discretize each asperity as in a small-scale core experiment. Yet, evaluating processes at the small scale allow for a better understanding of the complex processes leading to fracture deformation via THMC processes.

5. CONCLUSIONS

A range of behaviors was observed in our tests. We observed low permeability and low permeability change with dissolution and precipitation (granite) to large compaction with limited permeability change (rhyolite). Both of these types of measurements are indicative of fracture behavior and sustainability. For example, the rhyolite sample had the largest initial aperture of all samples tested, and in spite of no observed permeability change, showed the largest compaction. A longer-term test might have showed closure of the fracture, however could result in no change at all if dissolution results in a larger flow path. Variable permeability, in spite of very little indicated fracture closure from compaction was observed in the meta-sedimentary mudstone test. It is not clear what caused this, but may be indicative of some movement of fines either from mechanical or chemical processes in the aperture. The greatest change in permeability was indicated in the silicified rhyolite tuff, although the compaction was not as significant as the rhyolite tuff.

In addition to the expected dissolution from the use of aggressive distilled water, minerals were observed precipitating. It was not expected to see precipitation with such a low hydraulic residence time and distilled water. The minerals observed to precipitate formed small-high-surface area grains or plates. All precipitates appear to be detrimental to permeability because they lack mechanical strength and have high surface to volume ratios. SEM images from thin sections clearly show heterogeneous dissolution, and the mechanical

weakening of the near-fracture zone. Fundamental fluid mechanics tells us that fluid flow near asperities will be slower than in more open space in a fracture. This will limit the diffusive and advective removal of dissolved species, yet it will still result in weakening asperity contacts over time. The lack of mechanical strength in the precipitated material, and also in the near-fracture altered zone might indicate that asperity contacts will become weak, and the zones containing these precipitated minerals would be easily compressed, causing significant declines in permeability.

We have viewed our flow property changes using parallel-plate aperture or a wormhole end members. Neither of these two end members adequately describes flow in a real heterogeneous fracture. Wormholes would be less susceptible to mechanical closing, however are poor at exchanging heat, whereas the reverse is true for parallel-plate aperture. Nonuniform dissolution along an active flow path in a fracture would tend to produce wormholes. We have not seen this happen yet, however the duration of our tests may be too short for this to happen. Such longer term tests may not need to be performed under these experimentally difficult conditions.

Aperture observations have shown 1. little change, and 2. change that indicates the future formation of a worm-hole like high-permeability pathway. Further analysis of the initial and final conditions is needed to understand this better. Continued modeling of the tests is underway to gain a better idea of what happened in the experiments, and to build confidence in the models and codes. Additional modeling is adding to our understanding of the complex nature of the sustainability of fractures, yet more is needed to accurately incorporate the initial geometry of the asperity contacts as well as the mechanical and chemical processes.

Rock and aperture heterogeneity make determining the loaded initial geometry of the fracture exceedingly difficult, yet of necessity to model accurately geomechanical deformation and stress-mediated reactions leading to plastic strain at the core-scale. At field scales the fracture surface properties are only known at best on an average or statistical sense, so that modeling can capture the essential processes without having to discretize each asperity as in a small-scale core experiment. Evaluating processes at the small scale is still important as it allows for a better understanding of the complex processes leading to fracture deformation via THMC processes.

ACKNOWLEDGMENTS

This work was supported by the Assistant Secretary for Energy Efficiency and Renewable Energy (EERE), Office of Technology Development, Geothermal Technologies Program, of the U.S. Department of Energy under Contract No. DE-AC02-05CH11231. The meta-sedimentary, rhyolite and silicified tuff rock core samples and composition information were provided by Ormat Technologies, Inc.

REFERENCES

Ameli, P., J. E. Elkhoury and R. L. Detwiler (2013). "High-resolution fracture aperture mapping using optical profilometry." Water Resources Research **49**(10): 7126-7132.

Ayling, B., Rose, P., Petty, S., Zemach, E., and Drakos, P. (2012) QEMSCAN® (Quantitative evaluation of minerals by scanning electron microscopy): Capability and application to fracture characterization in geothermal systems. Proceedings, 37th Workshop on Geothermal Reservoir Engineering, Stanford University, SGP-TR-194, 11 p.

Auradou, H., Drazer, G., Boschan, A., Hulin, J-P., and Koplik, J. (2006), Flow channeling in a single fracture induced by shear displacement, Geothermics, 35(5 - 6), 576-588.

Borja, R.I., K.M. Sama, P.F. Sanz, (2003). On the numerical integration of three-invariant elastoplastic constitutive models, Comput. Methods Appl. Mech. Engng, 192, 1227-1258.

Chen, Z., Narayan, S.P., Yang, Z., and Rahman, S.S. (2000), An experimental investigation of hydraulic behaviour of fractures and joints in granitic rock, International Journal of Rock Mechanics and Mining Sciences, 37(7), 1061-1071.

Davatzes, N.C. and S. H. Hickman (2010), The Feedback Between Stress, Faulting, and Fluid Flow: Lessons from the Coso Geothermal Field, CA, USA, Proceedings World Geothermal Congress 2010, Bali, Indonesia, 25-29 April 2010

Deng, H., S. Molins, C. Steefel, D. DePaolo, M. Voltolini, L. Yang and J. Ajo-Franklin (2016). "A 2.5D Reactive Transport Model for Fracture Alteration Simulation." Environmental Science & Technology **50**(14): 7564-7571.

Elkhoury, J. E., P. Ameli and R. L. Detwiler (2013). "Dissolution and deformation in fractured carbonates caused by flow of CO2-rich brine under reservoir conditions." International Journal of Greenhouse Gas Control **16, Supplement 1**(0): S203-S215.

Fetterman, J. A. and N.C. Davatzes (2011), Evolution of Porosity in Fractures in the Newberry Volcano Geothermal System, Oregon, USA: Feedback between Deformation and Alteration, GRC Transactions, 35, 339-346.

Gentier, S., Lamontagne, E., Archambault, G., and Riss, J. (1997), Anisotropy of flow in a fracture undergoing shear and its relationship to the direction of shearing and injection pressure, International Journal of Rock Mechanics and Mining Sciences, 34(3 - 4), paper 094.

Kim, J, E. Sonnenthal, J. Rutqvist, (2012). Formulation and sequential algorithms of coupled fluid/flow and geomechanics for multiple porosity materials, Int. J. Numer. Meth. Engng, 92, 425-456. doi: 10.1002/nme.4340.

Kim J., Sonnenthal E., and Rutqvist J. (2015) A sequential implicit algorithm of chemo-thermo-poro-mechanics for fractured geothermal reservoirs. Computers & Geosciences, 76, 59–71.

Kneafsey, T. J., Nakagawa, S., Dobson, P. F., Borglin, S. E., Voltolini, M., Smith, J. T., Yang, L., and Sonnenthal, E. L. (2016). *Laboratory Determination of Fracture Sustainability in EGS Systems*. Paper presented at the 41st Workshop on Geothermal Reservoir Engineering, Stanford University, Stanford, California.

Kneafsey, T. J., S. Nakagawa, P. F. Dobson and B. M. Kennedy (2015). Fracture Sustainability in EGS Systems – Results of Laboratory Studies. Fourtieth Workshop on Geothermal Reservoir Engineering. Stanford University, Stanford, California, Stanford University**:** 676-684.

Kneafsey, T.J., S. Nakagawa, P.F. Dobson, B.M. Kennedy, J.P. Icenhower, and S. Nakashima, Sustainability of Fractures in EGS Systems – A Laboratory Investigation, (2014) Thirty-Ninth Workshop on Geothermal Reservoir Engineering, Stanford University, Stanford, California, February 24-26, 2014

Lutz, S.J., Hickman, S., Davatzes, N., Zemach, E., Drakos, P., and Robertson-Tait, A. (2010), Rock mechanical testing in support of well stimulation activities at the Desert Peak geothermal well, Nevada, Geothermal Resources Council Transactions, 34, 373-380.

Lutz, S.J., Zutshi, A., Robertson-Tait, A., Drakos, P., and Zemach, E. (2011), Lithologies, hydrothermal alteration, and rock mechanical properties in wells 15-12 and BCH-3, Bradys Hot Springs geothermal field, Nevada. Geothermal Resources Council Transactions, 35, 469-476.

Nemoto, K., N. Watanabe, N. Hirano, and N. Tsuchiya (2007), Evaluation of Flow Anisotropy Within a Simulated Shear Fracture Under Stress Conditions from Shallow to Deep Reservoirs, GRC Transactions, 31, 301-306.

Noiriel, C., P. Gouze and B. Madé (2013). "3D analysis of geometry and flow changes in a limestone fracture during dissolution." Journal of Hydrology **486**: 211-223.

Polak, A., Elsworth, D., Liu, J., and Grader, A.S. (2004), Spontaneous switching of permeability changes in a limestone fracture with net dissolution, Water Resour. Res., 40(3), W03502.

Polak, A., Elsworth, D., Yasuhara, H., Grader, A.S., and Halleck, P.M. (2003), Permeability reduction of a natural fracture under net dissolution by hydrothermal fluids, Geophys. Res. Lett., 30(20), 2020.

Roth, J. N.C. Davatzes, A.E.Krull Devatzes, (2013) Investigating the Volume and Structure of Porosity in Fractured and Unfractured Rock From the Newberry Volcano, Oregon, USA: Evaluation of Two- and Three-Dimensional Methods, GRC *Transactions*, Vol. 37

Olkiewicz, A., Gale, J.E., Thorpe, R., and Paulsson, B. (1979) Geology and fracture system at Stripa. Swedish-American cooperative program on radioactive waste storage in mined caverns in crystalline rock. Technical Information Report #21, LBL-8907, 164 p.

Smith, J.T. E.L. Sonnenthal, T. Cladouhos, (2015). Thermal-hydrological-mechanical modelling of shear stimulation at Newberry Volcano, Oregon, Amer. Rock Mech. Assn. 49th US Rock Mechanics/Geomechanics Symposium proceedings, 15-0680.

Sonnenthal, E.L., Spycher, N., Xu, T., Zheng, L., Miller, N., Pruess, K. (2014). TOUGHREACT V3.0-OMP, http://esd.lbl.gov/research/projects/tough/software/toughreact.html.

Swan, G., 1977. The Mechanical Properties of Stripa Granite, September, (1977), KBS Teknisk Rapport 48, Karnsbranslesakerht, reprinted as L.B.L. Report 7074, August,

TerraTek (2009) Petrologic evaluation of selected core and well samples – Desert Peak wells 35-13 TCH and 27-15 – Churchill County, Nevada. TR09-

TerraTek (2011) Petrologic evaluation of selected core samples – Bradys Hot Springs well BCH-03 – Churchill County, Nevada. TR11-403371.

Yasuhara, H., Elsworth, D., and Polak, A. (2004), Evolution of permeability in a natural fracture: Significant role of pressure solution, J. Geophys. Res., 109(B3), B03204.